JOURNAL OF MATERIALS SCIENCE 32 (1997) 5653–5659

Elastic–plastic indentation stress fields using the finite-element method

G. CARÈ*, A. C. FISCHER-CRIPPS
Department of Applied Physics, University of Technology, Sydney, PO Box 123, Broadway, NSW 2007, Australia

The finite-element method is used to model the elastic–plastic indentation response of a flat extensive specimen for the case of a spherical indenter. The work highlights several interesting finite-element modelling techniques and provides insight into the physical processes involved in elastic–plastic indentation of certain structural ceramics. Full details of the stress distribution are given and compared with the results of elastic formulae. This work has particular application to the modelling of physical phenomena of deformation in ceramic materials in machining, wear, bearings and hardness testing.

1. Introduction

The nature of the stresses arising from the contact between two elastic bodies is of considerable importance and was first studied by Hertz [1, 2] in 1881 (see also [3, 4]) before his more well-known work on electricity. Stresses arising from indentations with point loads, spheres, cylindrical flat punches, and diamond pyramids and cones are all of practical interest. The subsequent evolution of the field of contact mechanics has led to applications of the theory to a wide range of disciplines. The *elastic* stress fields generated by an indenter, whether it be a sphere, cylinder or cone, although complex, are well defined. When the response of the specimen material is *elastic–plastic* however, theoretical treatments [5–7] are limited because of the simplifying assumptions required to make such analyses tractable. In the following, we shall model the elastic–plastic indentation of a flat extensive specimen using the finite-element method. Since exact solutions, for an elastic response, are available in the literature, we shall use these as a basis for confirmation of the validity of our finite-element model and boundary conditions. We shall then use the finite-element method to model the elastic–plastic response of the specimen material and compare with experimentally observed phenomena. Experimental work to be presented concerns the indentation of a mica-containing machinable glass–ceramic available under the trade name Macor (Corning Inc., Corning, NY) [18]. This type of ceramic exhibits shear-driven subsurface accumulated damage in the indentation stress field [19]. We consider the case of loading with a spherical indenter. Although the indentation response of this material has been presented in the literature on previous occasions [20], we present here a full description of the elastic–plastic indentation stress fields together with details concerning the finite-element procedure.

2. Elastic theory

For the case of contact with a spherical indenter, the radius of the circle of contact between the indenter and the specimen surface increases with increasing load. For the purely elastic case, the contact area may be calculated using the Hertz relation

$$a^3 = \frac{4}{3}\frac{kPR}{E} \tag{1a}$$

where a is the radius of the circle of contact, P is the indenter load and R is the indenter radius. Equation 1a may be rearranged to give a linear relationship between the mean contact pressure $p_m = P/\pi a^2$ (the "indentation stress") and the ratio a/R (the "indentation strain"). In Equation 1a, k is an elastic mismatch parameter given by

$$k = \frac{9}{16}\left((1-\nu^2) + \frac{E}{E'}(1-\nu'^2)\right) \tag{1b}$$

In these equations, E and ν are the Young's modulus and Poisson's ratio, respectively, for the specimen, and E' and ν' the corresponding values for the indenter. The experimental indentation stress–strain response of the material may be used to calibrate the material properties of the specimen material for use in a finite element analysis. As reported previously [20], the slope of the linear portion of the response is proportional to the elastic modulus and any deviation from linearity may be used to estimate the yield stress and strain hardening coefficient.

**Present address*: G + D Computing Pty Ltd, 541 Kent Street, Sydney, NSW 2000, Australia.

0022–2461

For points within the interior of the specimen [21],

$$\frac{\sigma_r}{p_m} = \frac{3}{2}\left\{\frac{1-2\nu}{3}\frac{a^2}{r^2}\left[1-\left(\frac{z}{u^{1/2}}\right)^3\right]+\left(\frac{z}{u^{1/2}}\right)^3\frac{a^2u}{u^2+a^2z^2}\right.$$
$$\left.+\frac{z}{u^{1/2}}\left[u\frac{1-\nu}{a^2+u}+(1+\nu)\frac{u^{1/2}}{a}\times\tan^{-1}\left(\frac{a}{u^{1/2}}\right)-2\right]\right\} \quad (2)$$

$$\frac{\sigma_\theta}{p_m} = -\frac{3}{2}\left\{\frac{1-2\nu}{3}\frac{a^2}{r^2}\left[1-\left(\frac{z}{u^{1/2}}\right)^3\right]\right.$$
$$\left.+\frac{z}{u^{1/2}}\left[2\nu+u\frac{1-\nu}{a^2+u}-(1+\nu)\frac{u^{1/2}}{a}\times\tan^{-1}\left(\frac{a}{u^{1/2}}\right)\right]\right\} \quad (3)$$

$$\frac{\sigma_z}{p_m} = -\frac{3}{2}\left(\frac{z}{u^{1/2}}\right)^3\frac{a^2u}{u^2+a^2z^2} \quad (4)$$

$$\frac{\tau_{rz}}{p_m} = -\frac{3}{2}\frac{rz^2}{u^2+a^2z^2}\frac{a^2u^{1/2}}{a^2+u} \quad (5)$$

where

$$u = \frac{1}{2}\{(r^2+z^2-a^2)+[(r^2+z^2-a^2)^2+4a^2z^2]^{1/2}\} \quad (6)$$

In Equations 2–6, $p_m = P/\pi a^2$ is the mean contact pressure, with P equal to the indenter load, and a is the radius of the circle of contact.

The principal stresses in the r–z plane are given by

$$\sigma_{1,3} = \frac{\sigma_r+\sigma_z}{2} \pm \left[\left(\frac{\sigma_r-\sigma_z}{2}\right)^2+\sigma_{rz}^2\right]^{1/2}$$
$$\sigma_2 = \sigma_\theta \quad (7)$$
$$\tau_{max} = \tfrac{1}{2}(\sigma_1-\sigma_3)$$

and the angle between the direction of σ_1 and the surface of the specimen is given by

$$\frac{dz}{dr} = -\frac{\sigma_r-\sigma_z}{2\tau_{rz}} \pm \left[\left(\frac{\sigma_r-\sigma_z}{2\tau_{rz}}\right)^2+1\right]^{1/2} \quad (8)$$

where $\pm$ is the sign of τ_{rz} [21].

Contours of the normalized principal stresses and maximum shear stress calculated using Equations 2–7 above are shown in Fig. 1 together with the corresponding finite-element elastic–plastic solutions to be discussed below. In Fig. 1, distance scales have been normalized to the contact radius $a = a_0$ and stresses to the mean contact pressure, p_m, for the elastic solution.

3. Finite-element modelling technique

3.1. Contact between the indenter and the specimen

Contacts may be generally classified as being either conforming or non-conforming [22]. Loading with a cylindrical flat punch indenter is an example of a conforming contact since the contact area is a constant and independent of the load. Loading with a spherical or conical indenter is a non-conforming contact since the contact area is dependent on the load. However, this does not mean to say that contact involving such an indenter is a non-linear event. For frictionless contact, the contact area is completely specified in terms of linear elasticity as embodied in Equations 1 and 2. Thus, as far as finite-element modelling is concerned, we should obtain the same solution whether the load is applied in one step, or as a series of increments. The foregoing discussion assumes that all displacements are small. If this is not the case, then Equations 1 and 2 do not apply and, for finite-element modelling, non-linear *geometric* considerations must be included in the analysis. In the present work, we assume that such non-linear geometric considerations need not be considered for the purposes of comparison with the elastic theory but *are* included for the elastic–plastic analyses since they are significant when relatively large plastic strains are involved.

The solution of contact problems by finite-element analysis is often conveniently undertaken with the use of specialized gap elements. Although we have indicated that for frictionless contact a linear solution is obtained if the full indenter load is applied at once. modelling of the expanding area of contact, such as that required for spherical and conical indenters, does, however, require an iterative procedure. In the contact problem considered here, potential contacting surfaces are separated by specialized gap elements. The gap elements serve to prevent the "indenter" from overlapping the "specimen". An iterative procedure continually checks the status of each gap element, deleting and reinstating the element as required, until force equilibrium is reached within a specified tolerance level. Ideally, the gap elements should be assigned an infinite stiffness. This would ensure a non-intrusive contact between the indenter and the specimen. However, this is not possible in practice because of the finite numerical restrictions imposed by computer hardware. During contact, the indenter intrudes into the specimen a small amount given by the penalty factor. The penalty factor is the ratio of the stiffness of the gap elements to the stiffness of the specimen material. It is desirable at least to have the stiffness of the gap beams to be considerably larger than that of the specimen material. If the penalty factor is too low, then there is insufficient stiffness to enforce the contact condition. A penalty factor of about 10 000 was sufficient to simulate contact in the present case.

3.2. Elastic–plastic response

In the previous section, we argued that indentation with a spherical indenter in frictionless contact with a flat specimen surface is essentially a linear contact problem where the full load may be applied at once and the expanding area of contact determined using an iterative procedure. Linear solutions of this type may be applied to a non-linear material response by applying the load in increments where the response is assumed to be elastic within each increment.

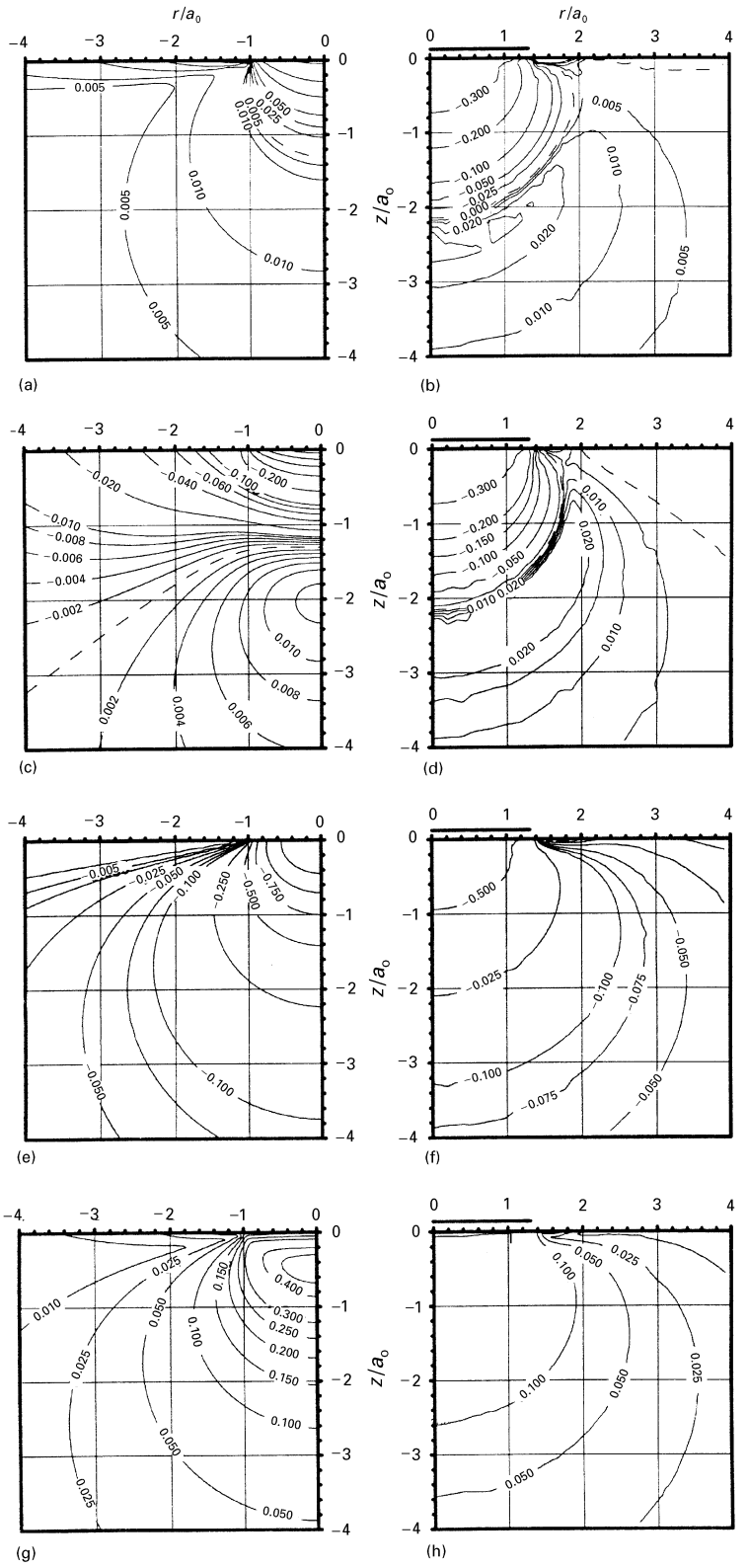

Figure 1 Contours of principal stress for Macor glass–ceramic material with spherical indenter: (a), (c), (e), (g), elastic solutions from Equations 2–8; (b), (d), (f), (h) finite-element results for elastic–plastic response. Magnitudes are shown for (a), (b) σ_1, (c), (d) σ_2, (e), (f) σ_3, and (g), (h) τ_{max}. For both elastic and elastic–plastic results, distances are expressed relative to the contact radius, $a_0 = 0.326$ mm, and stresses in terms of the mean contact pressure, $p_m = 3.0$ GPa, for the elastic case at $P = 1000$ N.

For material non-linearity, the local elastic modulus of each element is modified at each iteration for each load increment so as to satisfy a specified constitutive relationship. This is commonly referred to as the "secant" method of non-linear iteration. For example, in the present case, the shear-driven nature of the subsurface damage indicates an elastic–plastic response commonly observed in indentation testing of ductile materials. The shear-driven nature of the damage on a microstructural scale in the present case allows us to specify the Tresca shear stress yield criterion in the finite-element procedure.

The elastic–plastic properties of the specimen material in the finite-element model are specified by

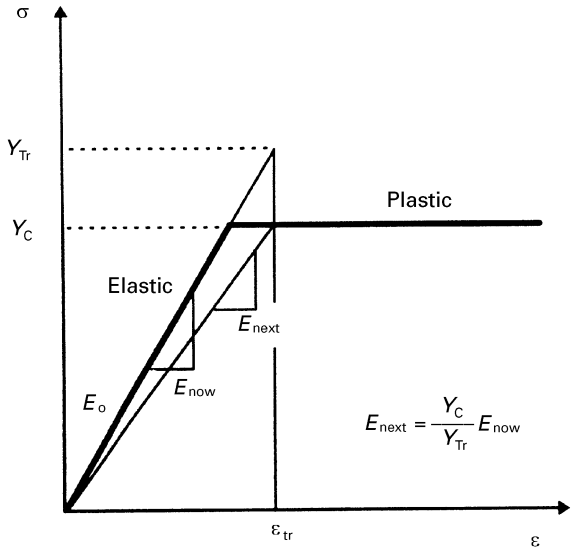

Figure 2 Elastic–plastic stress–strain curve showing iterative procedure used to satisfy the yield criterion. The elastic modulus of each element is adjusted so as to satisfy the specified uniaxial stress–strain relationship, here shown as elastic–perfectly plastic ($\beta = 0$).

a uniaxial stress–strain relationship. For an elastic –perfectly plastic material, the stress–strain relationship is that such as shown by the bold line in Fig. 2. Elastic–plastic behaviour is accommodated by first applying the load for the first increment with $E = E_0$ for all elements in the model. E_0 is the gradient of the stress–strain curve, specified in the element property set, at zero strain. Within each load increment, starting with the first increment, iterations are performed until the specified tolerance level is reached. Within each iteration, the modulus of elasticity for each element is adjusted so as to satisfy the chosen yield criterion.

Fig. 2 shows the procedure for a particular load increment. E_{now} is the initial stiffness for a particular element, which for the first iteration of the first load increment is E_0. In Fig. 2 this is shown as the stiffness prior to the application of the first load increment but may equally well represent the stiffness of a particular element after the analysis of a preceding load increment and series of iterations. For each element, the Tresca strain, ε_{Tr}, is calculated using E_{now}:

$$\varepsilon_{Tr} = \frac{Y_{Tr}}{E_{now}} \tag{9}$$

where

$$Y_{Tr} = \max\|\sigma_1 - \sigma_2|, |\sigma_2 - \sigma_3|, |\sigma_3 - \sigma_1\| \tag{10}$$

Y_{Tr} is compared with the yield stress, Y_c, obtained from the stress–strain curve at ε_{Tr}. If Y_{Tr} is greater than Y_C, then that element is carrying more stress than is permitted by the specified stress–strain curve and failure criterion. The modulus E_{now} for that element is then factored down an amount given by

$$E_{next} = E_{now} \frac{Y_C}{Y_{Tr}} \tag{11}$$

and a new solution calculated for that load increment with $E = E_{next}$. Iterations are performed until the values for Y_{Tr} agree, within a specified tolerance level, with those determined from the curve at a given ε_{Tr}.

The approach to plasticity described above is adequate for the purposes of the present analysis but is not suitable when one wishes to analyse the unloading. Here, we need to employ more sophisticated techniques such as the incremental strain, or incremental stress methods [23].

3.3. Finite-element model

A schematic diagram of a portion of the finite-element model used in the present work is shown in Fig. 3. The complete finite-element mesh consists of 1736 nodes and 1538 axis-symmetric quadrilateral plate elements. The outer dimensions of the model were some 150 times the radius of the circle of contact at the highest load increment. To enable direct comparison with experimental results, the indenter radius was set to 3.18 mm which resulted in a node spacing directly beneath the indenter of about 8 μm. The stiffness of the gap elements was set larger than that of the elements representing the specimen by a factor of about 1×10^6. During the solution, a maximum of 25 iterations per load increment were permitted and this was sufficient to obtain convergence with a force tolerance of 1% of the normalized residual force and 0.5% of the maximum normalized displacement. Load was applied in a series of steps up to the maximum specified load. A total of 20 load increments were specified. An updated Lagrangian method was employed within the finite-element code to account for the geometric non-linearity associated with large

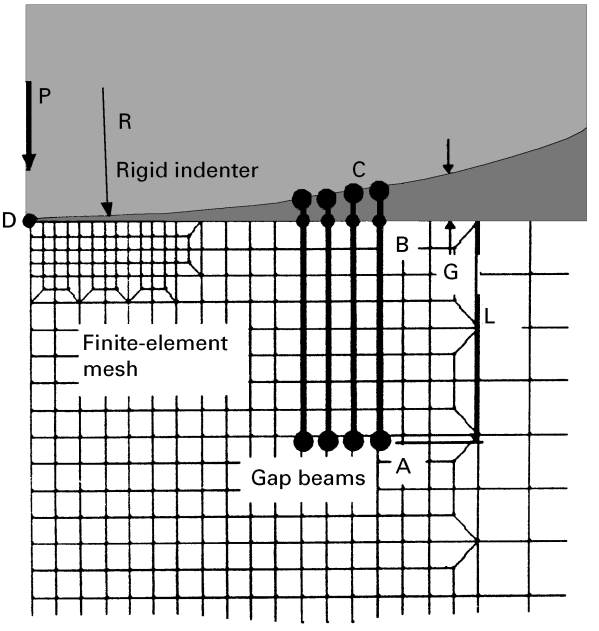

Figure 3 Detail of the finite-element mesh near prospective contact area. Four gap-beam elements are shown. Constraints and freedoms for nodes at C and A ensure that nodes at B and C move together when gap G closes during application of load.

TABLE I Mechanical properties of Macor glass–ceramic test material, where the elastic modulus, E, and yield stress, Y, were determined from the experimental indentation stress–strain relationship

Test material	Young's modulus, E (MPa)	Poisson's ratio, ν	Yield stress, Y (MPa)	E/Y
Macor	64 000	0.26	770	85

strains which may arise in the material in which yield has occurred.

Material properties, such as elastic modulus and yield stress, for the specimen material were determined by experiment using the indentation stress–strain response of the material [19, 20]. The elastic modulus, E, is found from the linear portion of the indentation stress–strain curve and the yield stress, Y, may be estimated from the value of mean contact pressure corresponding to the point of first deviation from linearity on such a curve. An indentation stress–strain curve is obtained by plotting values of mean contact pressure for a spherical indenter against a/R where a is the radius of the circle of contact and R is the radius of the spherical indenter.

The indentation response and corresponding values for elastic modulus, E, and yield stress, Y, for the glass–ceramic test material have been previously reported in the literature [20] and are given in Table I.

To test the accuracy of the finite-element models and associated boundary conditions, results for the fully elastic case were calculated and compared with the Hertz solution. The radius of the circle of contact estimated from the finite-element results agreed to within 1% of that calculated by Equation 1. The level of agreement obtained here was considered to be adequate for the purposes of the present investigation.

4. Experimental work

As has been previously reported [19, 20], the indentation response of certain ceramic materials is most vividly demonstrated by the nature of the subsurface damage beneath the indentation. Either the nature of the damage may be brittle, in which a characteristic Hertzian cone crack appears, or there may be evidence of shear-driven accumulated damage, similar to that observed in ductile materials. The nature of the subsurface damage may conveniently be observed using the bonded-interface or split-specimen technique. Full details of the method have been given in [19] and need not be repeated here.

A section view of the subsurface damage for the test material is shown in Fig. 4 together with the corresponding finite-element solution to be discussed below. The residual impression in the surface made by the indenter is clearly visible as is the shear-driven accumulated subsurface damage resulting from the indentation.

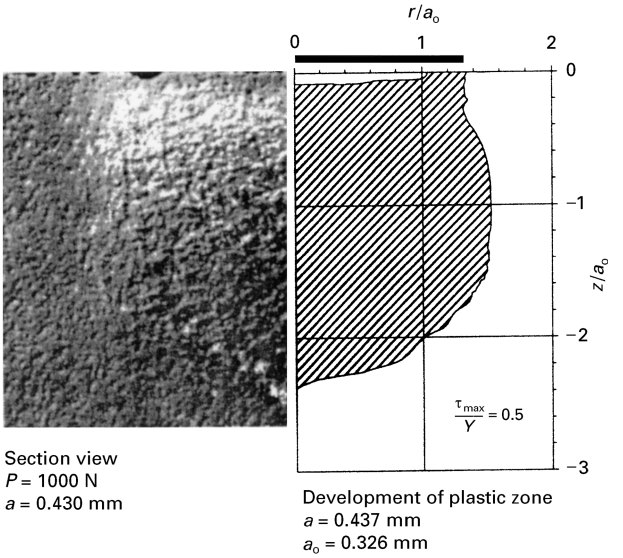

Figure 4 (a) Bonded-interface test result showing section view with subsurface accumulated damage beneath the indentation. (b) Finite-element result showing extent of the plastic zone in terms of contours of maximum shear stress at $\tau_{max}/Y = 0.5$ for indenter load $P = 1000$ N. Distances are expressed in terms of the contact radius, $a_0 = 0.326$ mm, for the elastic case of $P = 1000$ N. The bold black line indicates the radius of the circle of contact, $a = 0.437$ mm, as determined from the finite-element calculation.

5. Results and discussion

The present work demonstrates how the finite-element method may be used to solve a seemingly complex indentation problem with relatively simple modelling techniques. Although application of the finite-element method to elastic–plastic indentations with a spherical indenter is not new [23–29], we present here full details of the elastic–plastic indentation stress field for a material which is of particular interest to ceramicists. The subsurface damage exhibited by the material studied here arises because of the confined nature of the shear stress in the indentation stress field and is similar to that seen in traditional ductile materials [19, 20]. The corresponding indentation stress field provides information about possible crack paths within the material or regions of potential shear-driven "yield". Owing to the geometry of the plastic zone, conventional hardness theories (e.g., the so-called "expanding-cavity" model) are inappropriate [20] and information about the interior stresses can only conveniently be obtained using numerical techniques such as described here.

Comparison between experimental results and finite-element solutions is graphically demonstrated by the correspondence between the sub-surface damage or "yield" zones as shown in Fig. 5. This figure

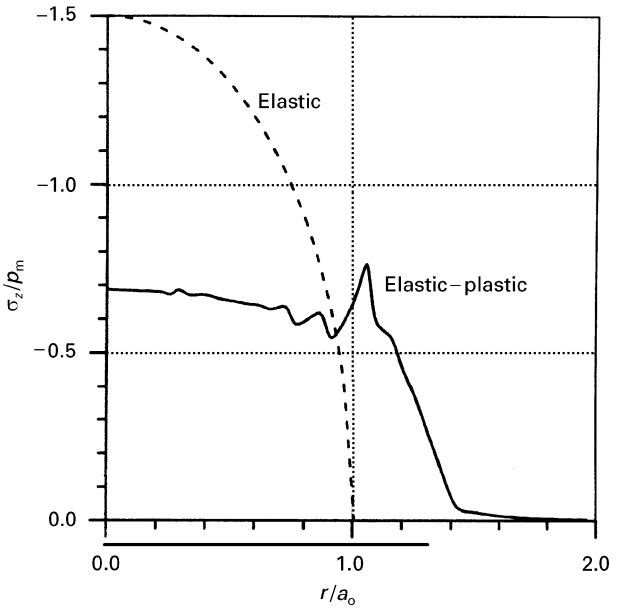

Figure 5 Contact pressure distribution for elastic (equation), and elastic–plastic (finite element) contact for $P = 1000$ N. Results are normalized to a_0 and p_m as in Fig. 1. The bar at the bottom of the horizontal axis indicates the radius of the circle of contact, $a = 0.437$ mm, for the elastic–plastic condition.

shows a contour of principal shear stress τ_{max} for a single value of $\tau_{max}/Y = 0.5$ which identifies the extent of the plastic zone (according to the Tresca criterion specified in the finite-element analysis). In this figure, the spatial coordinates have been expressed in terms of the radius of the circle of contact a_0 for the elastic solution at a load $P = 1000$ N. Absolute values may be obtained by multiplying the values indicated on the axes by $a_0 = 0.326$ mm.

Of particular interest is a comparison between the elastic and elastic–plastic stress distributions shown in Fig. 1. This figure shows that the presence of the "plastic" or damage zone significantly alters the near-field indentation stress field. In general, the magnitudes of the maximum principal stresses appear to shift outwards, away from the centre of contact when compared with the elastic case. The far-field stresses, however, appear to be little changed from the elastic case. The shift in magnitudes of stresses away from the centre of contact indicates a shift in the distribution of upward pressure which serves to support the indenter. This is reflected in the contact pressure distributions shown in Fig. 5, where the contact pressure for the elastic–plastic case appears to be more uniformly distributed (except for the rise in contact pressure near the edge of the contact circle) compared with the elastic case. In Fig. 1, results are plotted normalized to the mean contact pressure $p_m = 3.0$ GPa and contact radius $a_0 = 0.326$ mm for the elastic case. Absolute values may be obtained by multiplying by these factors.

Fig. 6 shows the variation in stress along the surface, and downwards along the axis of symmetry. As for Fig. 1, results are plotted normalized to the elastic contact pressure ($p_m = 3.0$ GPa) and contact radius ($a_0 = 0.326$ mm). Also shown in this figure are the results for the elastic solution for the maximum

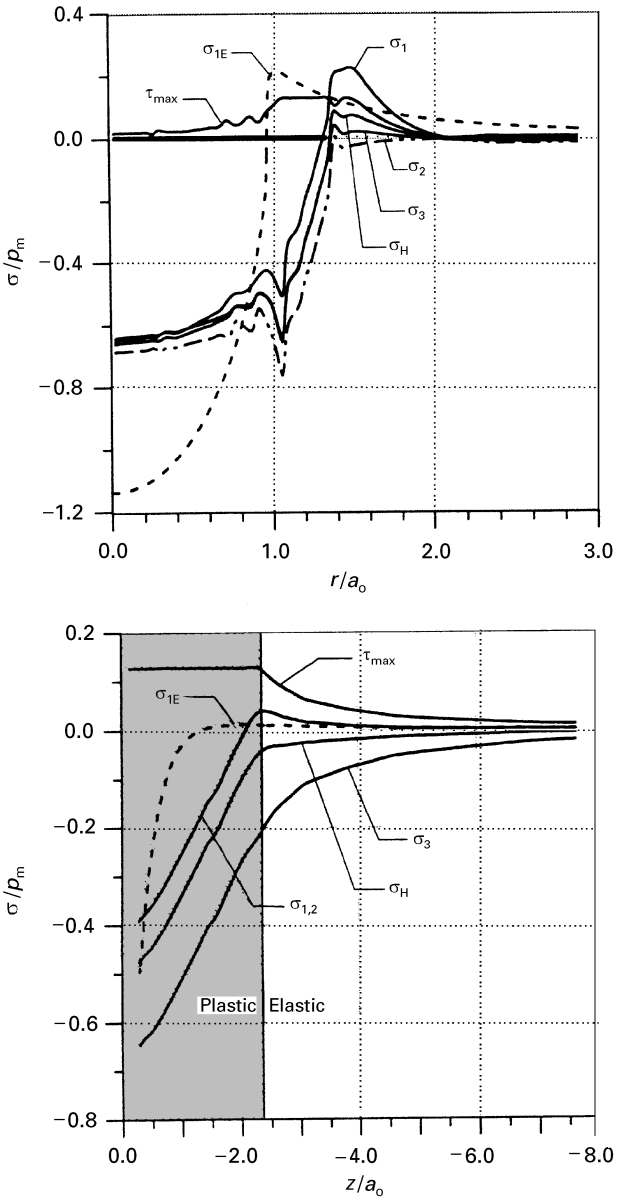

Figure 6 Variation in the stresses, σ_1, σ_2 and σ_3, the hydrostatic component, σ_H, and the maximum shear stress, τ_{max}, along (a) the surface of the specimen at $z = 0$ and (b) downwards along the axis of symmetry at $z = 0$. In both (a) and (b), the broken curve σ_{1E} shows the variation in σ_1 as calculated from elastic formulae for comparison with the elastic–plastic finite-element result. The horizontal bar in (a) indicates the radius of circle of contact, $a = 0.437$ mm, for the elastic–plastic condition. The shaded area in (b) indicates the region in which plastic strains have occurred.

principal stress, σ_1. As shown in Fig. 6a, along the surface the maximum value of σ_1 is very much the same as for the elastic case although the contact pressure is correspondingly lower owing to the larger area of contact in the elastic–plastic case (with $a = 0.437$ mm). There is an interesting change in magnitude for all stresses within the contact zone near the edge of the circle of contact. In a previous publication [20] it was shown that this arises because the plastic zone is contained within the area of the circle of contact and this discontinuity flattens out for contacts on materials, such as metals, where the plastic zone extends beyond the radius of circle of contact.

In Fig. 6b, the variation in stresses along the axis of symmetry downwards into the specimen material are

shown. Note that the maximum tensile stress occurs at the elastic–plastic boundary and is larger by a factor of about 3.6 than that calculated for an elastic contact.

The significance of these results is particularly important to those wishing to use indentation stress fields for structural reliability analysis. The failure of brittle materials is often attributed to the action of tensile stresses on surface flaws. For example, a procedure for determining the conditions for initiation of a Hertzian crack in soda–lime glass has been previously reported [30] and applies to a purely elastic contact. For the type of material studied here, i.e., a nominally brittle ceramic which undergoes shear-driven failure within a "plastic" zone, an analysis involving Weibull statistics may not be appropriate or, if it is, may need to be applied to flaws *within* the interior of the specimen rather than on the surface. Whatever analysis is selected, then a detailed knowledge of the state of stress within the material is required. Such details, for one particular class of ceramics, have been presented here.

Acknowledgements

Useful discussions with R. Dukino and M.V. Swain are gratefully acknowledged. This work was funded in part by the US Air Force Office of Scientific Research and the US National Institute of Standards and Technology.

References

1. H. HERTZ, *J. Reine Angew. Math.* **92** (1881) 156.
2. *Idem.*, in "Hertz's miscellaneous papers' Macmillan, London, 1896) Chapter 5. (translation and reprint in English of [1]).
3. F. AUERBACH, *Ann. Phys. Chem.* (*Leipzig*) **43** (1891) 61.
4. *Idem.*, in "Miscellaneous documents of the House of Representatives for the First Session of the Fifty-Second Congress", Vol. 43 (1891–1892) (Government Printing Office, Washington DC) p. 207.
5. R. HILL, E. H. LEE and S. J. TUPPER, *Proc. R. Soc. A* **188** (1947) 273.
6. R. HILL, "The mathematical theory of plasticity" (Clarendon, Oxford, 1950).
7. D. M. MARSH, *Proc. R. Soc. A* **279** (1964) 420.
8. L. E. SAMUELS and T. O. MULHEARN, *J. Mech. Phys. Solids* **5** (1957) 125.
9. T. O. MULHEARN, *ibid.* **7** (1959) 85.
10. K. L. JOHNSON, *J. ibid.* **18** (1970) 115.
11. M. C. SHAW and D. J. DESALVO, *Trans. ASME* **92** (1970) 469.
12. *Idem., ibid.* **92** (1970) 480.
13. M. V. SWAIN and J. T. HAGAN, *J. Phys. D* **9** (1976) 2201.
14. C. M. PERROTT, *Wear* **45** (1977) 293.
15. S. S. CHIANG, D. B. MARSHALL and A. G. EVANS, *J. Appl. Phys.* **53** (1982) 298.
16. *Idem., ibid.* **53** (1982) 312.
17. K. L. JOHNSON, "Contact mechanics" (Cambridge University Press, Cambridge, 1985).
18. D. G. GROSSMAN, *J. Amer. Ceram. Soc.* **55** (1972) 446.
19. H. CAI, M. A. STEVENS KALCEFF and B. R. LAWN, *J. Mater. Res.* **9** (1994) 762.
20. A. C. FISCHER-CRIPPS, *J. Mater. Sci.* (1996) in press.
21. M. BARQUINS and D. MAUGIS, *J. Mec. Theori. Appl.* **1** (1982) 331.
22. K. W. MAN, "Contact mechanics using boundary elements" (Computational Mechanics Publications, Southampton, Hants., 1994).
23. O. C. ZIENKIEWICZ and Y. K. CHEUNG, "The finite element method in structural and continuum mechanics" (McGraw-Hill, London, 1967).
24. S. R. WILLIAMS, "Hardness and hardness measurements" (American Society for Metals, Cleveland, OH, 1942).
25. C. HARDY, C. N. BARONET and G. V. TORDION, *Int. J. Numer. Methods Engng* **3** (1971) 451.
26. P. S. FOLLANSBEE and G. B. SINCLAIR, *Int. J. Solids Struct.* **20** (1981) 81.
27. R. HILL, B. STORAKERS and A. B. ZDUNEK, *Proc. R. Soc. A* **423** (1989) 301.
28. K. KOMVOPOULOS, *Trans. ASME* **111** (1988) 477.
29. *Idem. ibid.* **111** (1989) 430.
30. A. C. FISCHER-CRIPPS and R. E. COLLINS, *J. Mater. Sci.* **29** (1994) 2216

Received 9 October 1996
and accepted 1 May 1997